Materials Science & Engineering A 818 (2021) 141446

Contents lists available at ScienceDirect

Materials Science & Engineering A

journal homepage: www.elsevier.com/locate/msea

Remarkable strength of a non-equiatomic $Co_{29}Cr_{29}Fe_{29}Ni_{12.5}W_{0.5}$ high-entropy alloy at cryogenic temperatures

Chengbin Wei [a], Yiping Lu [a,*], Xinghao Du [b], Tingju Li [a], Tongmin Wang [a,**], Peter K. Liaw [c]

[a] Key Laboratory of Solidification Control and Digital Preparation Technology (Liaoning Province), School of Materials Science and Engineering, Dalian University of Technology, Dalian, 116024, China
[b] School of Materials Science and Engineering, Shenyang Aerospace University, Shenyang, 110136, China
[c] Department of Materials Science and Engineering, The University of Tennessee, Knoxville, TN, 37996, USA

ARTICLE INFO

Keywords:
High-entropy alloys
Dislocation
Stacking fault
Phase transformation
Mechanical properties

ABSTRACT

A non-equiatomic $Co_{29}Cr_{29}Fe_{29}Ni_{12.5}W_{0.5}$ high-entropy alloy (HEA) strengthened by two-step rolling was fabricated, and its microstructure evolution and tensile behavior at cryogenic temperatures were investigated. When the temperature decreases from 293 K to 173 K, the yield strength increases from 640 MPa to 1017 MPa. At 77 K, an outstanding strength-ductility synergy can be observed, with a yield strength of 1.33 GPa and an excellent ductility of 46%. Prior to tensile testing, the annealed alloy largely has a single face-centered cubic (FCC) structure, while a hexagonal-close packed (HCP) phase is formed in the cryogenically tensile-fractured alloy along the {111} planes. Such high yield strength and tensile plasticity values at cryogenic temperatures are extremely rare in HEAs and even in metal alloys. The deformation micro-mechanism was carefully investigated by a transmission electron microscope, and the results indicated that the cryogenic-temperature properties could be attributed to stacking faults (SFs) and the phase having a hexagonal-close-packed (HCP) structure. The densities of the SFs and the HCP laths have a considerable influence on the work-hardening behavior.

1. Introduction

Owing to their excellent properties, high-entropy alloys (HEAs), or multi-component alloys (MCAs) have appealed to researchers across the world since they were first proposed by Yeh et al. and Cantor et al. [1–3]. The configurational entropy helped some HEAs form simple solid solutions with face-centered-cubic (FCC), body-centered-cubic (BCC), or hexagonal-close-packed (HCP) structures [4,5]. Among the various HEAs, FCC-structured HEAs have the considerable disadvantage of low strengths at room temperature. To obtain HEAs with good ductility and high strength, many strategies have been adopted, such as introducing grain refinement [6,7], precipitation [8,9], phase transformations [10], and the use of heterogeneous microstructures [11,12].

The FCC-structured HEAs have dominated contemporary discussions on the deformation behavior of HEAs at low temperatures owing to their excellent mechanical properties. Gludovatz et al. found that the FCC-structured CoCrFeMnNi HEA had an excellent combination of strength, ductility, and fracture toughness at cryogenic temperatures, comparable to 316 stainless steel (SS) [13]. Moreover, later work showed that the CoCrNi medium-entropy alloy (MEA) was tougher than CoCrFeMnNi HEA at liquid nitrogen temperature [14]. It was indicated that the twinning mechanisms contributed to the remarkable strain hardening and mechanical properties of the CoCrNi MEA and CoCrFeMnNi HEA. Yang et al. designed a $Ni_{30}Co_{30}Fe_{13}Cr_{15}Al_6Ti_6$ dual-phase nano-composite-structured HEA that presented exceptional strength−ductility synergy at 77 K. Except for precipitation hardening, nano-spaced stacking faults (SFs) dominated the deformation mechanism and promoted the ductility and strain hardening of the HEA [15]. Also, several studies indicated that MEAs and HEAs with an FCC matrix at cryogenic temperatures achieved high ultimate tensile strength was contributed by the transformation induced plasticity effect [16,17].

The value of stacking fault energy (SFE) is an important factor related to the deformation of FCC alloys. It is known that the SFE will drop as the temperature decreases, and the formation of deformation twins, shear bands, SFs and martensitic transformation can be enhanced at cryogenic temperatures [18–20]. These additional deformation mechanisms, as well as dislocation slip, result in alloys with high fracture strength, large ductility and high strain hardening rate. However,

* Corresponding author.
** Corresponding author.
E-mail addresses: luyiping@dlut.edu.cn (Y. Lu), tmwang@dlut.edu.cn (T. Wang).

https://doi.org/10.1016/j.msea.2021.141446
Received 15 March 2021; Received in revised form 13 May 2021; Accepted 13 May 2021
Available online 20 May 2021

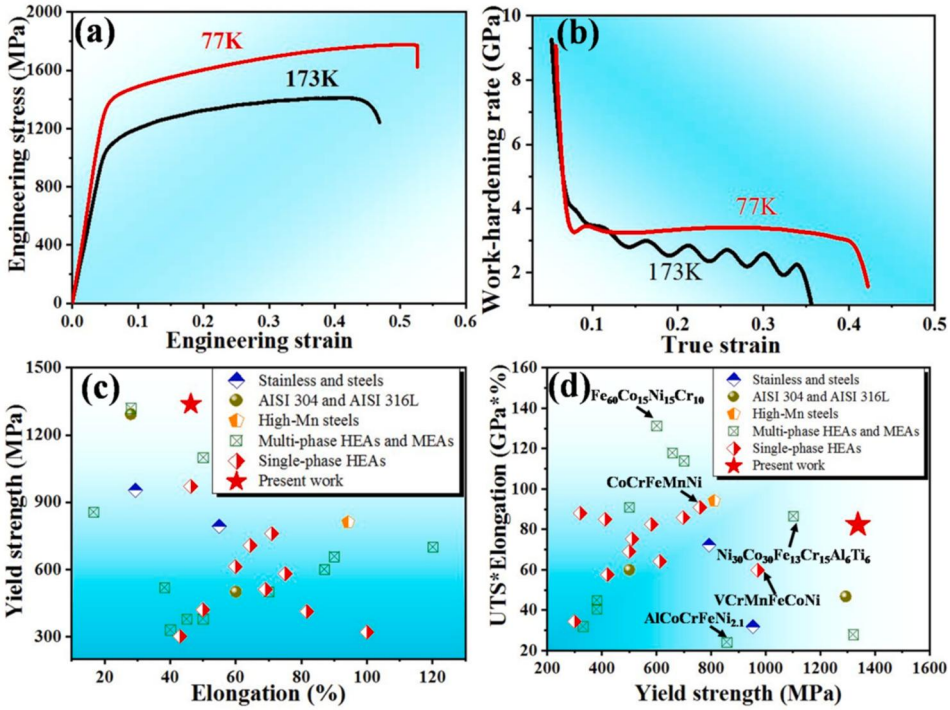

Fig. 1. Mechanical properties of the $Co_{29}Cr_{29}Fe_{29}Ni_{12.5}W_{0.5}$ alloy at low temperatures. (a) Engineering strain–stress curves of the tested alloy at 77 K and 173 K. (b) Work-hardening rate (WHR) versus true strain responses of the alloy at 77 K and 173 K. Comparison of yield strength versus elongation (c) and mechanical properties (d) of the alloy with other typical alloys at 77 K [13–17,22–34].

the low yield strength (YS) of FCC-structured HEAs restricted their use in cryogenic applications, such as high-strength fasteners, high-performance gears, and nuclear reactors.

In our previous work, a novel $Co_{29}Cr_{29}Fe_{29}Ni_{12.5}W_{0.5}$ alloy was designed that had a favorable combination of strength and ductility at room temperature [21]. In order to study the microstructural evolution and mechanical properties at low temperatures, uniaxial tensile tests on $Co_{29}Cr_{29}Fe_{29}Ni_{12.5}W_{0.5}$ HEA were conducted at various low temperatures. The mechanical behavior and microstructures of the alloy at different temperatures were investigated. The alloy shows excellent properties at cryogenic temperature. The deformation mechanisms of the alloy at low temperatures were discussed in detail.

2. Experimental methods

Alloy ingots with a nominal composition of $Co_{29}Cr_{29}Fe_{29}Ni_{12.5}W_{0.5}$ (atomic percent, at.%) were produced by melting a mixture of pure metals (purity ≥99.95 wt percent, wt.%) in a high-purity argon atmosphere in a vacuum-induction furnace. The molten alloy was cast in a Cu mold to form a rectangular bulk sample with a length of 75 mm, width of 15 mm and thickness of 12 mm. The sample was first homogenized at 1,473 K for 2 h and subsequently water quenched. It was then hot rolled to reduce the thickness by 30% at 1,173 K. After hot rolling, the alloys were homogenized again at 1,473 K for 2 h, followed by water quenching. Subsequently, the alloys were cold-rolled to sheets of 2 mm thickness. The cold-rolled sheets were then annealed at 1,073 K for 60 min, followed by immediate water quenching. A more detailed description can be found in our earlier work [21].

Flat dog-bone tensile specimens were cut from the annealed sheets by electric discharge machining along the rolling direction, with a gauge length of 25 mm, width of 4 mm, and thickness of 2 mm. Tensile tests were carried out, using an Instron 5582 machine with a strain of 10^{-3} s^{-1} at 77 K, 173 K, and 293 K, respectively. For the experiments at 77 K, the specimens and grip were completely immersed in liquid nitrogen for 15 min before the tensile test. The testing was stopped at engineering strains of 10%, 25%, and 35%, respectively. In order to ensure that the tensile specimens are held at the target temperature, the specimens were always submerged in liquid nitrogen during testing. These interrupted tensile tests, together with the complete tensile tests in liquid nitrogen, help elucidate the microstructure evolution during tensile deformation.

Fracture-surface morphologies after tensile deformation were identified by scanning electron microscopy (SEM, SUPARR 55). The X-ray diffraction (XRD) measurements were conducted on an Empyrean machine (PANalytical B. V.) with Cu-Kα radiation at 40 kV and 30 mA to analyze the crystal structures of the annealed and fractured alloys. The scanning range was between 30° and 100° (2θ) with a step size of 6°/min. The evolution of the microstructure during tensile deformation was characterized by transmission electron microscopy (TEM, JEOL, 2100F). The specimens for TEM investigations were prepared by mechanical polishing, followed by twin-jet electro-polishing (electrolyte: 93% ethanol + 7% perchloric acid in terms of volume percent). Electron backscatter diffraction (EBSD) measurements were performed, using a TESCAN MAIA3-XMH SEM equipped with the OXFORD Nordlys Max data collection software.

3. Results

3.1. Mechanical properties

Fig. 1 (a) shows the engineering strain–stress curves of the alloy at 173 K and 77 K. The alloy has an outstanding combination of strength and ductility both at 173 K and 77 K. Both the YS and ultimate tensile strength (UTS) increase significantly when the deformation temperature decreases from 293 K to 77 K. For instance, the YS is increased by 109% from 640 MPa to 1,338 MPa, and the UTS is increased by 72% from 1,031 MPa to 1,780 MPa. Meanwhile, the strength increases sharply with only little loss in ductility, resulting in a property profile that is beyond the inverse strength–ductility relation under cryogenic conditions. For example, the uniform tensile elongation (El) is 55.4% at 293 K [21]. When the temperature decreased to 173 K and 77 K, the El are

Table 1
Yield strength (YS), ultimate tensile strength (UTS), and uniform elongation (El) obtained at 293 K [21], 173 K, and 77 K.

Temp. (K)	YS (MPa)	UTS (MPa)	El (%)
293	640	1,031	55.4
173	1,017	1,410	40.6
77	1,338	1,780	46.3

40.6% and 46.3%, respectively. The strength and ductility of the $Co_{29}Cr_{29}Fe_{29}Ni_{12.5}W_{0.5}$ alloy at various temperatures are provided in Table 1 for comparison.

Fig. 1 (b) depicts the work-hardening rate (WHR) curves at low temperatures. The alloy exhibits different work hardening behavior between 173 K and 77 K. At 77 K, the WHR exhibits a rapid decrease in the early deformation stage, followed by a slight increase, and subsequently, a decrease at the last stage. When the strain reached 0.4, the WHR still remained approximately 3 GPa. However, at 173 K, the WHR shows a monotonous decrease with the strain accompanied by some fluctuations. Fig. 1 (c) and (d) present the mechanical properties of other classic HEAs/MEAs and steels at 77 K [13–17,22–34]. Compared with other alloys, the $Co_{29}Cr_{29}Fe_{29}Ni_{12.5}W_{0.5}$ alloy exhibits excellent properties at cryogenic temperature as indicated by the red stars in Fig. 1 (c) and (d). It could be found that the mechanical properties of the alloy at low temperature are desirable and rare in HEAs/MEAs and even in steels.

The fracture morphologies of the samples after tensile testing at 173 K and 77 K were examined, and the results are shown in Fig. 2. From Fig. 2 (a) and (d), it can be seen that there is slight necking at 173 K but no obvious macroscopic necking at 77 K, proving that the samples deformed uniformly during the testing process. There are no features of brittle fracture at either 173 K or 77 K. All samples show evidence of dimpled fracture, but their dimple sizes are dramatically different. The dimple morphology is similar in both the edge and center regions of the tensile sample deformed at 173 K, as presented in Fig. 2 (b) and (c). The average size of the dimples is approximately 1 μm. However, in Fig. 2 (e) and (f), the dimples in the sample deformed at 77 K are not uniform. They show a gradual decrease from the center to the edge. The dimples in the sample have a much smaller size and a higher density in the edge region. The ultrafine dimples have an approximate average size of 2 μm in the central region (Fig. 2 (e)), while the edge regions have much smaller dimples with an average size of approximately 600 nm (Fig. 2 (f)). However, there are also a few coarser and deeper dimples at both the edge and the central regions in the samples deformed at 173 K and 77 K. Another important character is that micro-cracks were observed in the central region (indicated with white arrows in Fig. 2 (b) and (e)) but not in the edge region.

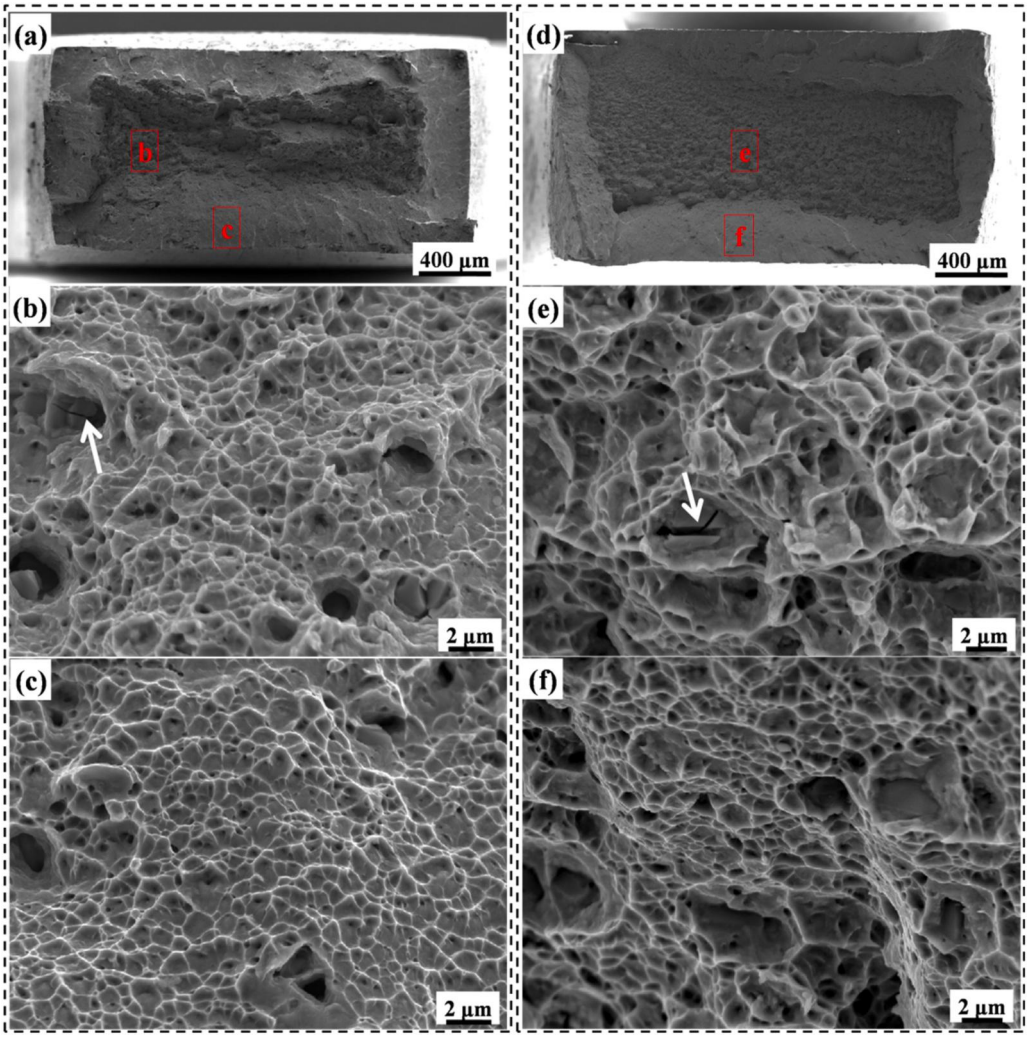

Fig. 2. Fracture morphologies of $Co_{29}Cr_{29}Fe_{29}Ni_{12.5}W_{0.5}$ alloy samples deformed at 173 K and 77 K. (a, d) Fracture morphologies of the alloy samples after tensile testing at 173 K and 77 K, respectively. (b, c) Enlarged images for central and edge regions of the fracture-surface marked in (a). (e, f) Enlarged images for central and edge regions of the fracture-surface marked in (b). White arrows in (b) and (e) highlight the micro-cracks in the central region.

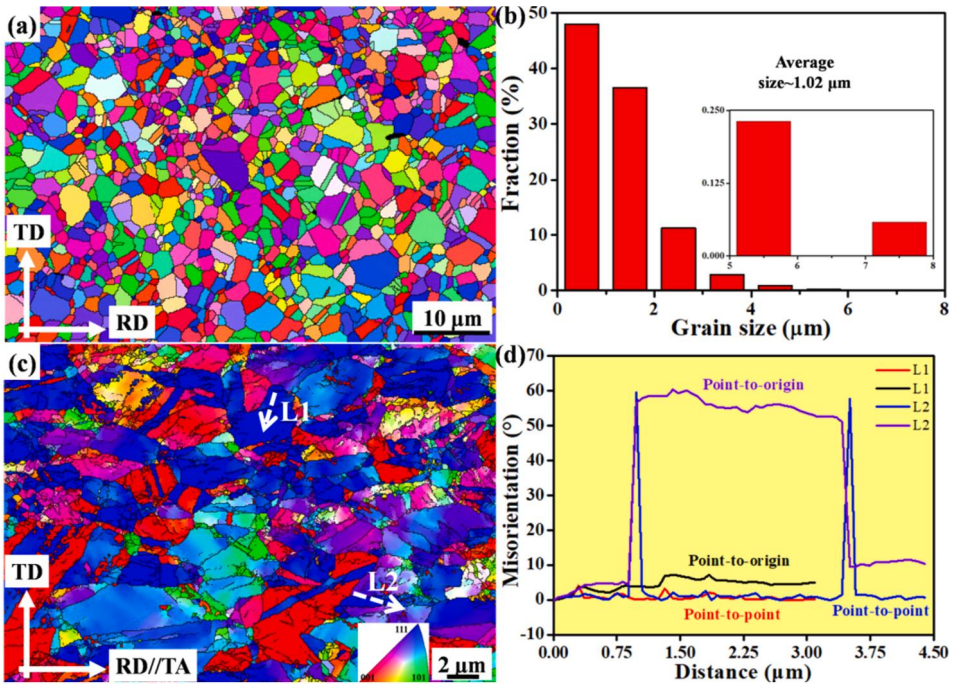

Fig. 3. EBSD results of the alloy annealed at 1,073 K and after a tensile test at 77 K. (a) IPF map of the alloy after annealing at 1,073 K. (b) Grain-size distribution of the 1,073 K-annealed alloy. (c) IPF map obtained in the region near the fracture area after tensile testing at 77 K. (d) Corresponding misorientation–distance curve for the dashed white arrows of the alloy after tensile at 77 K. The L1 and L2 represent the arrows in (c). The tensile axis (TA) is parallel to the rolling direction (RD). The transverse direction (TD) is perpendicular to the RD.

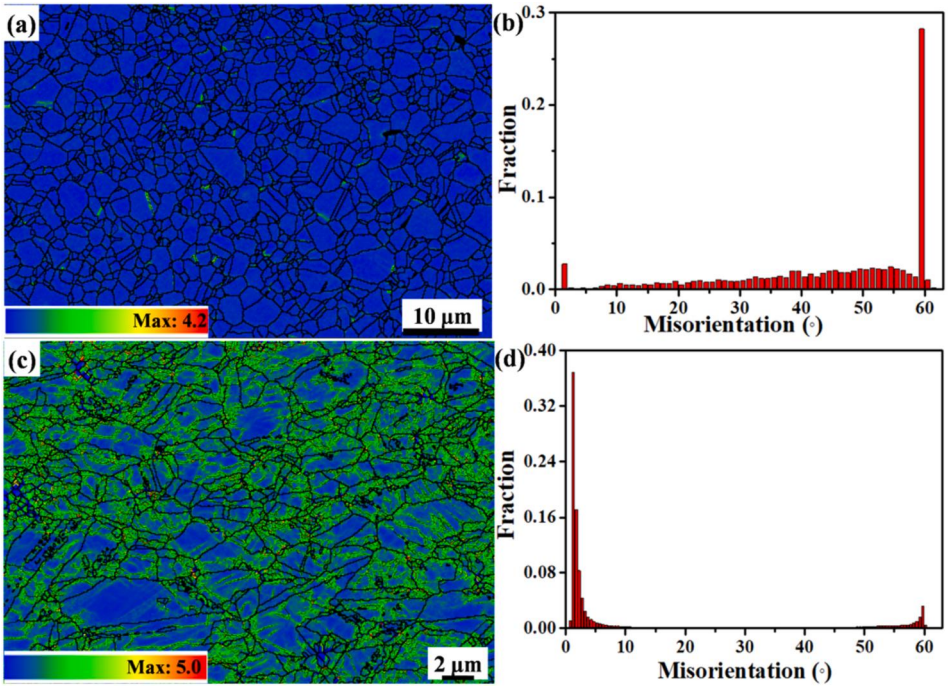

Fig. 4. (a) KAM map and (b) misorientation-angle distributions map of the 1,073 K-annealed alloy. (c) KAM map and (d) misorientation-angle distributions map of the alloy after a tensile test at 77 K.

3.2. Microstructures

To understand the evolution of microstructures during cryo-deformation of the alloy, the microstructure of the alloy before and after cryo-deformation were investigated. Fig. 3 presents EBSD maps of the alloy samples before and after tensile testing at 77 K. Before the uniaxial tensile tests, the annealed alloy has equiaxed grains with non-uniform grain sizes. The inverse pole figure (IPF) map is exhibited in Fig. 3 (a). The grain size varies from 0.2 to 8 μm, and the average grain size is approximately 1.02 μm (Fig. 3 (b)). After the tensile test at 77 K, many substructures or deformation structures were formed in the grains and annealing twins (as shown in Fig. 3 (c)). The misorientation along the white arrows L1 and L2 in the IPF map (Fig. 3 (c)) was shown in Fig. 3 (d). It suggests that the misorientation angle were increased both in the grains and the annealing twins. And the maximum misorientation is about 8° for L1. Fig. 4 shows the kernel average misorientation (KAM) and misorientation angle distributions maps before and after the tensile tests. The 1,073 K-annealed alloy with fine recrystallized grains has exceptionally low KAM values and a large number of high angle grain boundaries (HAGBs), as shown in Fig. 4 (a) and (b). After tensile testing

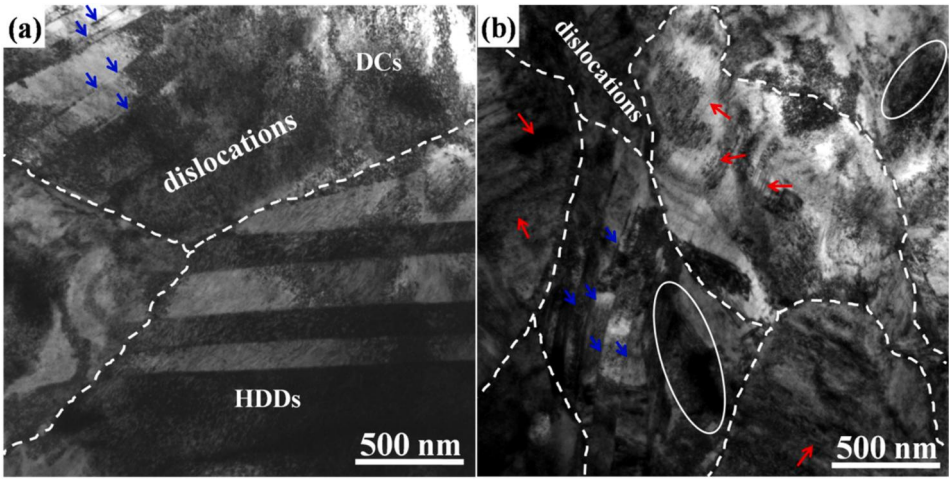

Fig. 5. BF images of the fractured microstructure of the alloy tensile at 173 K (a) and 77 K (b). The grain boundaries highlighted by white dashed lines.

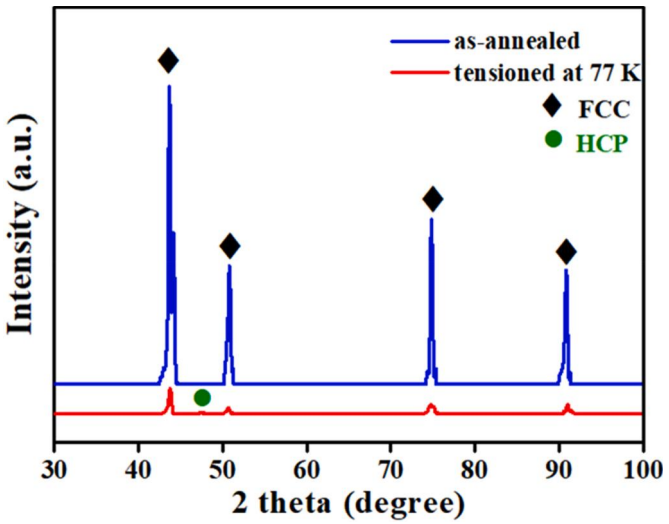

Fig. 6. XRD patterns of the alloy for the as-annealed and tensioned at 77 K states.

at 77 K, the KAM map reveals that the strain localization at grain boundaries and twin boundaries is higher than in the other regions, as observed in Fig. 4 (c). It is indicated that more dislocations were piled up at the boundaries and resulted in high KAM values. A large number of low-angle grain boundaries (LAGBs) were visible instead of the HAGBs in the sample, as shown in Fig. 4 (d), which can be further confirmed from the IPF map in Fig. 3 (c).

Fig. 5 presents the deformation microstructures of the fractured alloy after tensile testing at 173 K and 77 K. After being subjected to tension at 173 K, the TEM observation indicates that the recrystallized grains are characterized by dislocation cells (DCs), twins, and high-density dislocations (HDDs) (Fig. 5 (a)). The twin thickness is approximately 100 nm, and the twin spacing varies from 100 to 200 nm, respectively. HDDs within the twins and the dislocation pile up could be seen at the grain boundaries and twin boundaries. Some small, thin deformation structures with a spacing of nearly 150 nm could be found in the grains (marked with blue arrows in Fig. 5 (a)). Fig. 5 (b) shows the bright-field (BF) image of the fractured microstructure of the tensile alloy at 77 K. Except for the dislocation pileup at the grain boundaries and twin boundaries, there are some nano-spaced SFs within the grains (marked with red arrows in Fig. 5 (b)). In addition, a large number of dislocations is observed in the non-twin and non-SF areas (marked with white ellipses in Fig. 5 (b)). The twin thickness and spacing are smaller than the ones corresponding to the tension at 173 K (marked with blue arrows in Fig. 5 (b)). Meanwhile, the dislocations became tangled up and interacted with the twin boundaries. In fact, a large number of HCP plates, several nanometers in dimension are formed. The XRD patterns for the states of the as-annealed and tensioned samples at 77 K are shown in Fig. 6. The details will be discussed in the later section.

4. Discussion

4.1. Deformation behavior

Fig. 7 shows the deformation microstructures obtained by TEM for the alloy undergoing different strains at the liquid nitrogen temperature. At low (10%) strains, dislocation glide dominates the plastic deformation with dislocation pile-ups at the grain boundaries and twin boundaries, as indicated by the white circles in Fig. 7 (a). The Shockley partial dislocations with an SF in-between were observed and marked with red arrows in Fig. 7 (a). When the strain is further increased, the grains are dominated by SFs with much smaller spacing. The interaction between the dislocation and SFs may also be observed, and these are marked with red arrows in Fig. 7 (b). The HDD regions are formed in the SF-free regions marked with a white ellipse in Fig. 7 (b). When the sample was further strained to 35%, both the dislocation and the SF density increase considerably. The SF networks (see Fig. 7 (c)) were formed by intersected SFs. When the sample was further strained to failure (strained to 46%), the SF multiplied and the density of the HCP plates increased continuously. In addition to the SF networks, dislocation slip and SF-slip intersection were observed and marked with red arrows in Fig. 7 (d). High-density dislocation was observed along the grain boundary, suggesting that dislocation slip has an important role in the development of the desirable mechanical-property profile.

At the initial stage of deformation, the dislocation slip and SFs dominated the deformation. The SFs were formed by the interaction between different dislocations [35]. These SFs often provide continuous nucleation sites for mechanical twins and ε-martensite with further increase in the stress. With increasing strain, the spacing was decreased, and SF networks were formed by multiple SFs along the {111} plane (see Fig. 8 (a)). High resolution transmission electron microscopy (HRTEM) (see Fig. 8 (b)) indicates that the HCP phase with thickness equivalent to several atomic layers (marked with red dots) and SFs (marked with blue dashed lines) are formed along the {111} plane. After being fractured, a larger number of HCP plates appear, and the spacing of SF is reduced, as shown in Fig. 9 (a). There is an orientation relationship between the FCC matrix and HCP phase, $\{111\}_{FCC} \parallel \{0001\}_{HCP}$ and $[011]_{FCC} \parallel$

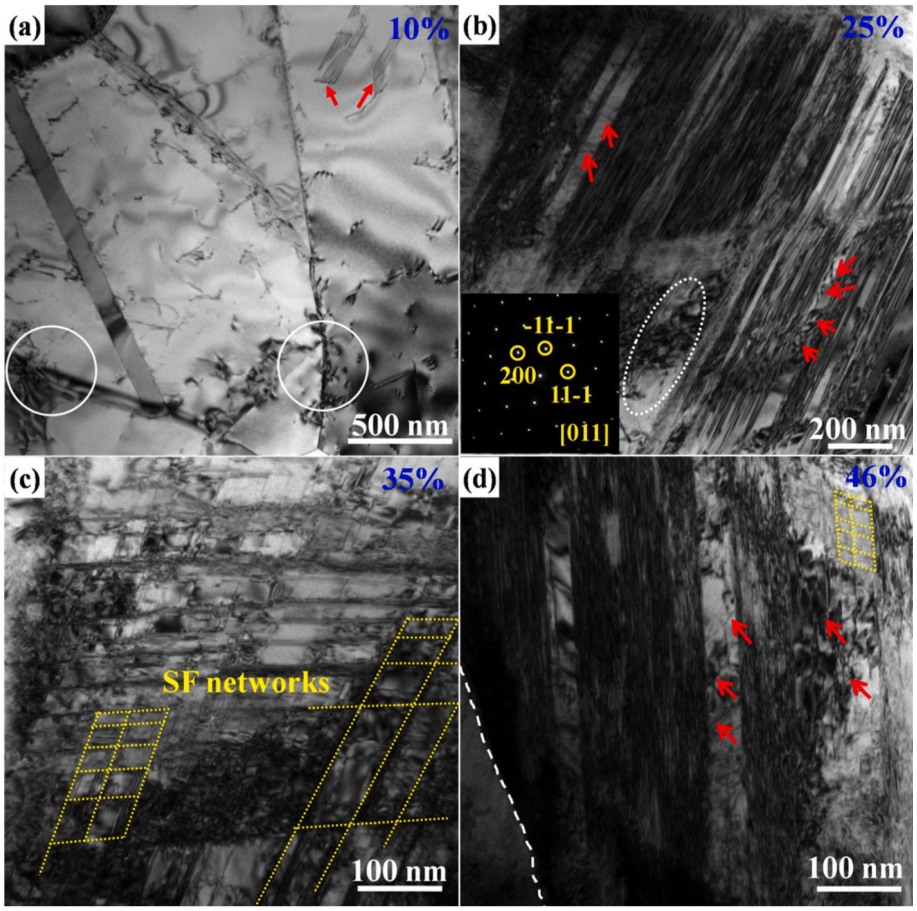

Fig. 7. BF images of the alloy after strains of (a) 10%, (b) 25%, (c) 35%, and (d) 46% at 77 K. The inset selected area electron diffraction (SAED) pattern in (b) show that the area has a single-phase FCC structure. The grain boundaries are highlighted by the white dashed line in (d).

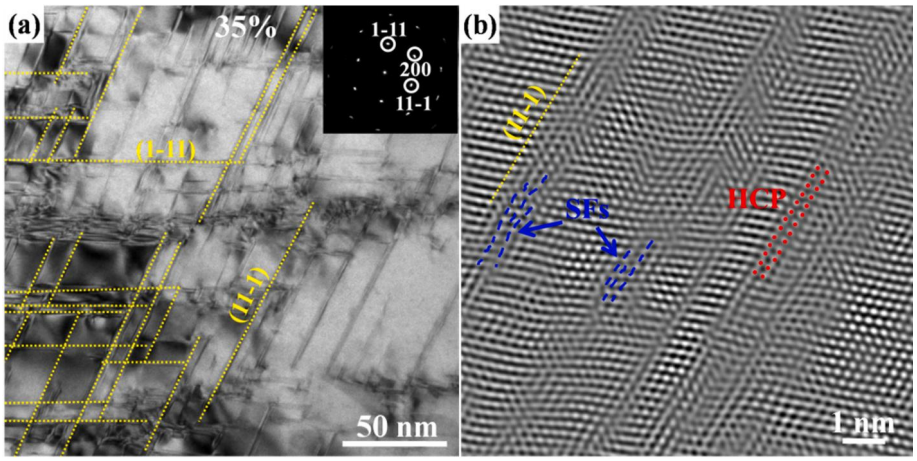

Fig. 8. BF (a) and HRTEM (b) image of the alloy after a strain of 35% at 77 K. Inset at top right-hand side of (a) is the SAED pattern of the BF image.

$[11–20]_{HCP}$, which corresponds to a typical Shoji-Nishiyama (S–N) relationship [36], as presented in Fig. 9 (b). It is well known that the SFs play an important role in twinning and martensite transformation as the precursors of nucleation [35,37–39]. The model developed by Fujita et al. [35] suggested that the reaction between the SFs and adjacent dislocations promotes the propagation and superposition of these SFs, and forms the HCP phase. Mahajan [39] and Wang et al. [40] proposed that two perfect dislocations in different lattice orientations of the same crystal plane group first react to form partial dislocations, and subsequently form twins and HCP phases with several atomic layers. In the present work, the formation of dislocation and SFs are observed in the FCC matrix marked with blue solid lines in Fig. 9 (c). No mechanical twins could be observed along the HCP plate phase (Fig. 9 (c) and (d)). Moreover, the reaction between the dislocations/SFs and dislocations have been observed in the TEM results (see Figs. 7 and 9). The results indicate that the ε-martensite transformation in the alloy under cryogenic conditions is in accordance with Fujita's model.

Like the deformation at 77 K, both the SFs and the HCP phase were

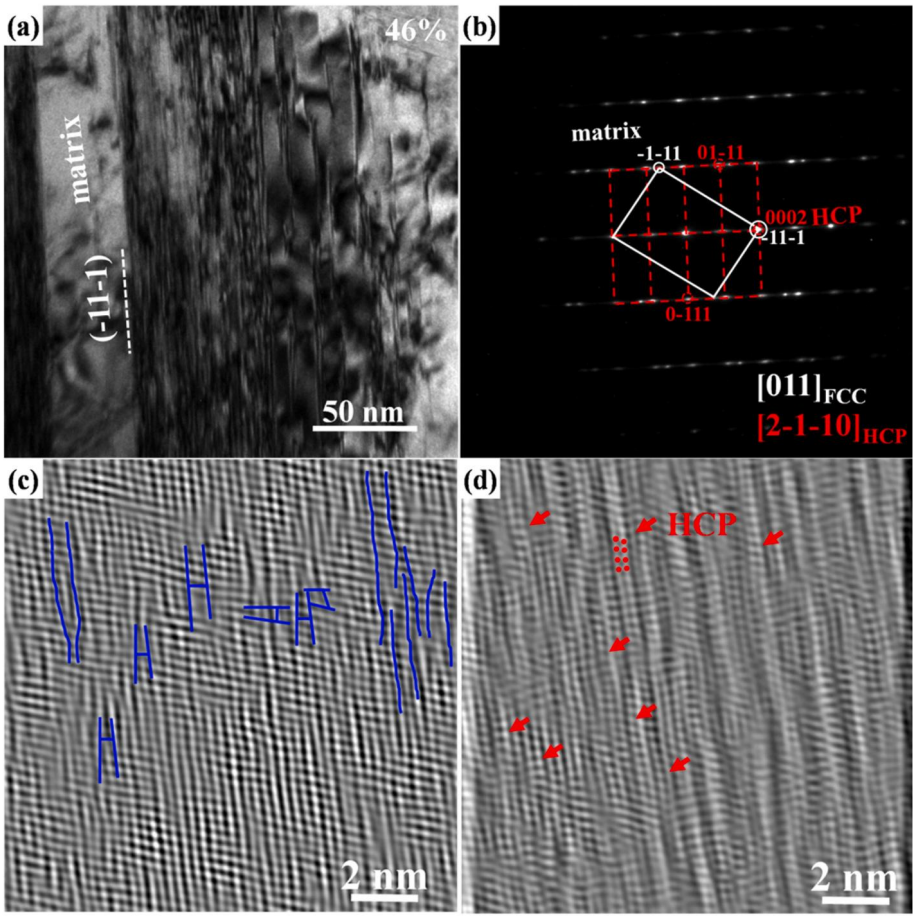

Fig. 9. TEM images of the alloy after tensile fracture at 77 K. (a) BF image of the alloy after tensile failure at 77 K. (b) SAED pattern of (a). (c) and (d) are the HRTEM images of the FCC matrix and HCP structure in (a), respectively.

observed in the samples that were strained up to failure at 173 K (see Fig. 10 (a)). The orientation relationship between the FCC matrix and HCP lamellae correspond to the S–N type (see Fig. 10 (b)). The relationship indicates that the formation of the HCP phase is related to the glide of Shockley partial dislocations on the {111} planes. When the SFs and Shockley partial dislocations encounter each other, it leads to dislocation stacking, and stress concentration occurs. The interaction between the SFs and dislocations or the overlap of SFs driven by the stress concentration result in the formation of HCP laths on the {111} planes [35,41] as observed in Fig. 10 (c) and (d). The formation mechanism of the HCP phase at 173 K is the same as that at 77 K.

However, for the sample deformed at 77 K, the densities of SFs and HCP phases are higher than those at 173 K. The SFE decreases as the temperature decreases and the lower the temperature, the lower the value of SFE [18,29]. Hence, a lower temperature enabled the introduction of a higher density of SFs and HCP plates.

4.2. Strengthening mechanisms and work-hardening behavior

In both alloys, the YS increases with the decrease in temperature. The YS increased from 1,017 MPa to 1,338 MPa when the temperature decreased from 173 K to 77 K. The increase in YS ($\Delta\sigma_{YS}$) of polycrystalline materials can be expressed as [8]:

$$\Delta\sigma_{YS} = \Delta\sigma_{ss} + \Delta\sigma_{gb} + \Delta\sigma_{pi} + \Delta\sigma_{p} \quad (1)$$

where $\Delta\sigma_{ss}$, $\Delta\sigma_{gb}$, $\Delta\sigma_{pi}$, and $\Delta\sigma_{p}$ are the contributions from the solid solution, grain boundary, initial dislocation density, and precipitates, respectively. In the present study, the $\Delta\sigma_{p}$ can be ignored as there were no precipitates. It is indicated that the initial dislocation density is exceptionally low due to recrystallization of the grains, and thus, the $\Delta\sigma_{pi}$ effect on the strength can almost be ignored. The average grain size of the alloy is approximately 1.02 μm, which contributes to the YS of the alloy. Hence, the $\Delta\sigma_{ss}$ and $\Delta\sigma_{gb}$ become the main factors that contribute to the increase of YS with the decreasing temperature. The increase in YS can be obtained as:

$$\Delta\sigma_{YS} = \Delta\sigma_{ss} + \Delta\sigma_{gb} \quad (2)$$

According to the Hall-Petch relationship, the second term on the right-hand side of the above equation can be written as:

$$\Delta\sigma_{gb} = \sigma_{0,T1} + k_{T1}d^{-1/2} - \sigma_{0,T2} - k_{T2}d^{-1/2}$$

$$= (\sigma_{0,T1} - \sigma_{0,T2}) + (k_{T1} - k_{T2})d^{-1/2} \quad (3)$$

where d is the grain size, and $\sigma_{0,T1}$, k_{T1}, $\sigma_{0,T2}$, and k_{T2} are the lattice friction stress and Hall-Petch slope at temperatures of T1 and T2, respectively. The Hall-Petch slope can be fitted using the following equation [42]:

$$k = \beta G b^{1/2} \quad (4)$$

where β is a constant, b is the Burgers vector, and G is the shear modulus, respectively. Combining Equations (3) and (4), Equation (3) becomes:

$$\Delta\sigma_{gb} = (\sigma_{0,T1} - \sigma_{0,T2}) + (G_{T1} - G_{T1})\beta b^{1/2} d^{-1/2} \quad (5)$$

where G_{T1} and G_{T2} are the shear moduli at temperatures of T1 and T2, respectively. The shear modulus, G, is slightly temperature-dependent [43]. Hence, the second term on the right side of Equation (5) can be

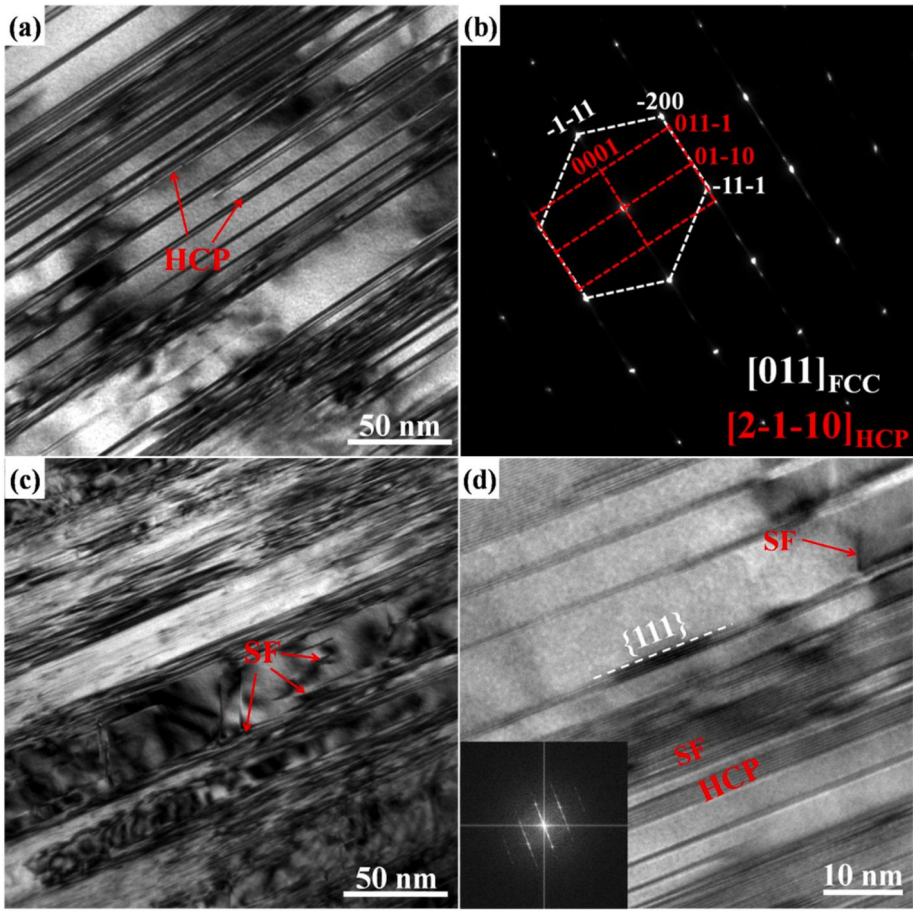

Fig. 10. BF TEM micrographs and the corresponding SAED pattern of the alloy after a tensile test at 173 K. (a) BF image of an HCP phase, (b) SAED pattern of (a), (c) BF image of SFs, (d) HRTEM image of the HCP phase and SFs. The inset is the fast Fourier transform pattern of the HRTEM image.

ignored and the main contribution of $\Delta\sigma_{gb}$ is the increase in the lattice friction stress.

According to Wu et al. [33], solution hardening can be incorporated into the lattice friction stress. Hence, Equation (2) can be written as:

$$\Delta\sigma_{YS} = N\Delta\sigma_T \tag{6}$$

where $\Delta\sigma_T$ is the increase of the lattice friction stress caused by the temperature, and N is a constant. Hence, the temperature dependence of the YS was dominated by lattice friction. The Peierls-Nabarro (P–N) stress (σ_p), which was controlled by the influence of temperature on the width of the dislocations, dominated the lattice friction. The value of σ_p could be calculated using the following equation [33]:

$$\sigma_p = \frac{2G}{1-\vartheta} exp(\frac{-2\pi\omega_0}{b})^* exp(\frac{-2\pi\omega_0}{b}\alpha T) \tag{7}$$

where ϑ is the Poisson's ratio, ω_0 is the dislocation width at 0 K, α is a positive constant, and T is the test temperature, respectively. The equation implies that the P–N stress would be amplified by the test temperature, while the YS remains the same. Moreover, Okamoto's study also suggested that the thermal component of solid-solution hardening contributed to the increase in the yield stress of FCC alloys at cryogenic temperatures [44].

As shown in Fig. 1 (b), the sample deformed at 77 K shows higher WHR than the sample deformed at 173 K at the early stage of deformation. The WHR drops rapidly in the early stage as the dislocations dominate the plastic deformation during the deformation process. This deformation behavior is like FCC metals, which may be attributed to the dynamic recovery of dislocations [29,45,46]. With the further increase in the strain, the WHR decreased slowly. The SFE will drop at a low temperature, which encourages the formation of more SFs. These SFs will impede the slip of other dislocations on the slip planes crossing the SF plane, which contributes to the WHR. As the strain increases, the SF density increases while the WHR increases slightly and remains high. A higher SF density implies a smaller dislocation-free path and stronger promotion of the WHR response by the dynamic Hall-Petch effect, which is similar to the TWIP effect [46–48]. Furthermore, as the strain increases, the formation of HCP laths will create more defective configurations like phase boundaries. The dislocations pile up at the phase boundaries during plastic deformation and cause a significant back stress that may further enhance the WHR [49,50]. In fact, the phase transformation induced in the region of stress concentration releases the stress concentration and delays the strain localization, thereby contributing to the uniform deformation.

At 173 K, the work-hardening behavior is different from the sample deformed at 77 K. The SFE is also higher than that at 77 K. The density of the SFs and HCP lath are lower than at 77 K (see Fig. 10). The phenomenon is similar to the results of the previous study observed in steels and FCC-structured HEAs [10,51,52]. The lower SF density means a coarser SF spacing size and dislocation-free path. Therefore, the promotion of WHR present in the alloy is weaker. Similar to the early deformation stage, the WHR drops due to the slip of dislocations. Dislocations encounter the SFs and pile up along the SFs or interact with them, and local internal stress concentrations are developed. A much greater external stress will be needed to overcome the concentrated stress. Such a process enhanced the work-hardening ability and exhibited the increase of WHR. Therefore, the WHR shows a fluctuating downward trend until failure.

5. Conclusions

In this study, the mechanical properties and microstructural evolution of the $Co_{29}Cr_{29}Fe_{29}Ni_{12.5}W_{0.5}$ alloy under cryogenic temperatures (173 K and 77 K) were investigated. Electron back scattered diffraction and transmission electron microscopy imaging investigations were used to reveal the outstanding mechanical properties and deformation mechanisms responsible for the different deformation stages. The main conclusions can be summarized as follows:

(1) The mechanical properties of the alloy showed a strong dependence on the temperature. The yield and ultimate strength at 173 K were 1,017 MPa and 1,410 MPa, while the values at 77 K were 1,338 MPa and 1,780 MPa, respectively. The mechanical properties were found to be superior to most of the reported alloys at cryogenic temperatures.
(2) Except for grain-boundary strengthening, solid-solution hardening (lattice friction) which is dominated by the P–N stress was the main factor for the high YS at cryogenic temperatures.
(3) The deformation of the alloy was dominated by dislocation slip, SFs, and phase transformation. These deformation mechanisms contributed to the high work-hardening rate and excellent mechanical properties at cryogenic temperatures.

CRediT authorship contribution statement

Chengbin Wei: Conceptualization, Investigation, Methodology, Writing – original draft, Validation. **Yiping Lu:** Writing – review & editing, Supervision. **Xinghao Du:** Formal analysis, Methodology. **Tingju Li:** Supervision. **Tongmin Wang:** Supervision, Funding acquisition. **Peter K. Liaw:** Writing – review & editing, Funding acquisition.

Declaration of competing interest

The authors declare that they have no known competing financial interests or personal relationships that could have appeared to influence the work reported in this paper.

Acknowledgements

The present work was supported by the Special Fund for Research on National Major Research Instrument (No. 51927801), the National Key Research and Development Program of China (Grant No. 2017YFA0403803, 2019YFA0209901 and 2018YFA0702901), the fund of the State Key Laboratory of Solidification Processing in NWPU (Grant No. SKLSP201902), the Liao Ning Revitalization Talents Program (XLYC1807047), and the Fund of Science and Technology on Reactor Fuel and Materials Laboratory (STRFML-2020-04). P. K. L. very much appreciates the supports from (1) the U.S. National Science Foundation [DMR-1611180 and 1809640] with the program directors, Drs. Judith Yang, Gary Shiflet, and Diana Farkas and (2) the Army Office Project [W911NF-13-1-0438 and W911NF-19-2-0049] with the program managers, Drs. Michael P. Bakas, David M. Stepp, and S. Mathaudhu.

References

[1] J.W. Yeh, S.K. Chen, S.J. Lin, J.Y. Gan, T.S. Chin, T.T. Shun, C.H. Tsau, S.Y. Chang, Nanostructured high-entropy alloys with multiple principal elements: novel alloy design concepts and outcomes, Adv. Eng. Mater. 6 (2004) 299–303.
[2] B. Cantor, I.T.H. Chang, P. Knight, A.J.B. Vincent, Microstructural development in equiatomic multicomponent alloys, Mater. Sci. Eng. 375–377 (2004) 213–218.
[3] Y. Zhang, T.T. Zuo, Z. Tang, M.C. Gao, K.A. Dahmen, P.K. Liaw, Z.P. Lu, Microstructures and properties of high-entropy alloys, Prog. Mater. Sci. 61 (2014) 1–93.
[4] D.B. Miracle, O.N. Senkov, A critical review of high entropy alloys and related concepts, Acta Mater. 122 (2017) 448–511.
[5] C. Zhang, M.C. Gao, High-entropy Alloys: Fundamentals and Applications, Spring International Publishing, 2016.
[6] S.W. Wu, G. Wang, J. Yi, Y.D. Jia, I. Hussain, Q.J. Zhai, P.K. Liaw, Strong grain-size effect on deformation twinning of an Al0.1CoCrFeNi high-entropy alloy, Mater. Res. Lett. 5 (2017) 276–283.
[7] W. Wu, M. Song, S. Ni, J. Wang, Y. Liu, B. Liu, X. Liao, Dual mechanisms of grain refinement in a FeCoCrNi high-entropy alloy processed by high-pressure torsion, Sci. Rep. 7 (2017) 46720.
[8] J.Y. He, H. Wang, H.L. Huang, X.D. Xu, M.W. Chen, Y. Wu, X.J. Liu, T.G. Nieh, K. An, Z.P. Lu, A precipitation-hardened high-entropy alloy with outstanding tensile properties, Acta Mater. 102 (2016) 187–196.
[9] K. Ming, X. Bi, J. Wang, Realizing strength-ductility combination of coarse-grained Al0.2Co1.5CrFeNi1.5Ti0.3 alloy via nano-sized, coherent precipitates, Int. J. Plast. 100 (2018) 177–191.
[10] Z. Li, K.G. Pradeep, Y. Deng, D. Raabe, C.C. Tasan, Metastable high-entropy dual-phase alloys overcome the strength-ductility trade-off, Nature 534 (2016) 227–230.
[11] M. Yang, D. Yan, F. Yuan, P. Jiang, E. Ma, X. Wu, Dynamically reinforced heterogeneous grain structure prolongs ductility in a medium-entropy alloy with gigapascal yield strength, Proc. Natl. Acad. Sci. U.S.A. (2018) 2–7.
[12] S.W. Wu, G. Wang, Y.D. Jia, J. Yi, Q.J. Zhai, C.T. Liu, B.A. Sun, H.J. Chu, J. Shen, P. K. Liaw, T.Y. Zhang, Enhancement of strength-ductility trade-off in a high-entropy alloy through a heterogeneous structure, Acta Mater. 165 (2019) 444–458.
[13] B. Gludovatz, A. Hohenwarter, D. Catoor, E.H. Chang, E.P. George, R.O. Ritchie, A fracture-resistant high-entropy alloy for cryogenic applications, Science 345 (2014) 1153–1158.
[14] B. Gludovatz, A. Hohenwarter, K.V.S. Thurston, H. Bei, Z. Wu, E.P. George, R. O. Ritchie, Exceptional damage-tolerance of a medium-entropy alloy CrCoNi at cryogenic temperatures, Nat. Commun. 7 (2016) 10602.
[15] T. Yang, Y.L. Zhao, J.H. Luan, B. Han, J. Wei, J.J. Kai, C.T. Liu, Nanoparticles-strengthened high-entropy alloys for cryogenic applications showing an exceptional strength-ductility synergy, Scripta Mater. 164 (2019) 30–35.
[16] J.W. Bae, J.B. Seol, J. Moon, S.S. Sohn, M.J. Jang, H.Y. Um, B.J. Lee, H.S. Kim, Exceptional phase-transformation strengthening of ferrous medium-entropy alloys at cryogenic temperatures, Acta Mater. 161 (2018) 388–399.
[17] D.G. Kim, Y.H. Jo, J. Yang, W.M. Choi, H.S. Kim, B.J. Lee, S.S. Sohn, S. Lee, Ultrastrong duplex high-entropy alloy with 2 GPa cryogenic strength enabled by an accelerated martensitic transformation, Scripta Mater. 171 (2019) 67–72.
[18] S. Huang, W. Li, S. Lu, F. Tian, J. Shen, E. Holmström, L. Vitos, Temperature dependent stacking fault energy of FeCrCoNiMn high entropy alloy, Scripta Mater. 108 (2015) 44–47.
[19] S. Zhao, G.M. Stocks, Y. Zhang, Stacking fault energies of face-centered cubic concentrated solid solution alloys, Acta Mater. 134 (2017) 334–345.
[20] D.T. Pierce, J.A. Jiménez, J. Bentley, D. Raabe, J.E. Wittig, The influence of stacking fault energy on the microstructural and strain-hardening evolution of Fe-Mn-Al-Si steels during tensile deformation, Acta Mater. 100 (2015) 178–190.
[21] C.B. Wei, Y.P. Lu, X.H. Du, J. Wang, T.M. Wang, Effects of deformation and annealing on the microstructures and properties of a nonequiatomic Co29Cr29Fe29Ni12.5W0.5 high-entropy alloy, Mater. Sci. Eng. (2020) 140548.
[22] H.S. Shin, H.M. Lee, M.S. Kim, Impact tensile behavior of 9% nickel steel at low temperature, Int. J. Impact Eng. 24 (2000) 571–581.
[23] P. Czarkowski, A.T. Krawczynska, R. Slesinski, T. Brynk, J. Budniak, M. Lewandowska, K.J. Kurzydlowski, Low temperature mechanical properties of 316L type stainless steel after hydrostatic extrusion, Fusion Eng. Des. 86 (2011) 2517–2521.
[24] C. Zheng, W. Yu, Effect of low-temperature on mechanical behavior for an AISI 304 austenitic stainless steel, Mater. Sci. Eng. 710 (2018) 359–365.
[25] S.S. Sohn, S. Hong, J. Lee, B.C. Suh, S.K. Kim, B.J. Lee, N.J. Kim, S. Lee, Effects of Mn and Al contents on cryogenic-temperature tensile and Charpy impact properties in four austenitic high-Mn steels, Acta Mater. 100 (2015) 39–52.
[26] P. Czarkowski, A.T. Krawczyńska, T. Brynk, M. Nowacki, M. Lewandowska, K. J. Kurzydłowski, Cryogenic strength and microstructure of a hydrostatically extruded austenitic steel 1.4429 (AISI 316LN), Cryogenics 64 (2014) 1–4.
[27] D. Li, C. Li, T. Feng, Y. Zhang, G. Sha, J.J. Lewandowski, P.K. Liaw, Y. Zhang, High-entropy Al0.3CoCrFeNi alloy fibers with high tensile strength and ductility at ambient and cryogenic temperatures, Acta Mater. 123 (2017) 285–294.
[28] D. Li, Y. Zhang, The ultrahigh charpy impact toughness of forged AlxCoCrFeNi high entropy alloys at room and cryogenic temperatures, Intermetallics 70 (2016) 24–28.
[29] F. Otto, A. Dlouhý, C. Somsen, H. Bei, G. Eggeler, E.P. George, The influences of temperature and microstructure on the tensile properties of a CoCrFeMnNi high-entropy alloy, Acta Mater. 61 (2013) 5743–5755.
[30] Z. Wu, C.M. Parish, H. Bei, Nano-twin mediated plasticity in carbon-containing FeNiCoCrMn high entropy alloys, J. Alloys Compd. 647 (2015) 815–822.
[31] T. Bhattacharjee, R. Zheng, Y. Chong, S. Sheikh, S. Guo, I.T. Clark, T. Okawa, I. S. Wani, P.P. Bhattacharjee, A. Shibata, N. Tsuji, Effect of low temperature on tensile properties of AlCoCrFeNi2.1 eutectic high entropy alloy, Mater. Chem. Phys. 210 (2018) 207–212.
[32] M.J. Jang, H. Kwak, Y.W. Lee, Y. Jeong, J. Choi, Y.H. Jo, W.M. Choi, H.J. Sung, E. Y. Yoon, S. Praveen, S. Lee, B.J. Lee, M.I. Abd El Aal, H.S. Kim, Plastic deformation behavior of 40Fe–25Ni–15Cr–10Co–10V high-entropy alloy for cryogenic applications, Met. Mater. Int. 25 (2019) 277–284.
[33] Z. Wu, H. Bei, G.M. Pharr, E.P. George, Temperature dependence of the mechanical properties of equiatomic solid solution alloys with face-centered cubic crystal structures, Acta Mater. 81 (2014) 428–441.
[34] Y.H. Jo, S. Jung, W.M. Choi, S.S. Sohn, H.S. Kim, B.J. Lee, N.J. Kim, S. Lee, Cryogenic strength improvement by utilizing room-temperature deformation

twinning in a partially recrystallized VCrMnFeCoNi high-entropy alloy, Nat. Commun. (2017) 1–8.
[35] H. Fujita, S. Ueda, Stacking faults and f.c.c. (γ) → h.c.p. (ε) transformation in 18 8-type stainless steel, Acta Metall. 20 (1972) 759–767.
[36] Morris E. Fine, M. Meshii, C.M. Wayman, Martensitic Transformation Zenji Nishiyama, Academic Press, INC., New York, 1978.
[37] I. Karaman, H. Sehitoglu, Y.I. Chumlyakov, H.J. Maier, I.V. Kireeva, Extrinsic stacking faults and twinning in Hadfield manganese steel single crystals, Scripta Mater. 44 (2001) 337–343.
[38] B. Uzer, S. Picak, J. Liu, T. Jozaghi, D. Canadinc, I. Karaman, Y.I. Chumlyakov, I. Kireeva, On the mechanical response and microstructure evolution of NiCoCr single crystalline medium entropy alloys, Mater. Res Lett. 6 (2018) 442–449.
[39] S. Mahajan, M.L. Green, D. Brasen, A model for the FCC→HCP transformation, its applications, and experimental evidence, Metall. Trans. A. 8 (1977) 283–293.
[40] M. Wang, Z. Li, D. Raabe, In-situ SEM observation of phase transformation and twinning mechanisms in an interstitial high-entropy alloy, Acta Mater. 147 (2018) 236–246.
[41] K. Ming, W. Lu, Z. Li, X. Bi, J. Wang, Amorphous bands induced by low temperature tension in a non-equiatomic CrMnFeCoNi alloy, Acta Mater. 188 (2020) 354–365.
[42] Z.C. Cordero, B.E. Knight, C.A. Schuh, Six decades of the Hall–Petch effect – a survey of grain-size strengthening studies on pure metals, Int. Mater. Rev. 61 (2016) 495–512.
[43] A. Haglund, M. Koehler, D. Catoor, E.P. George, V. Keppens, Polycrystalline elastic moduli of a high-entropy alloy at cryogenic temperatures, Intermetallics 58 (2015) 62–64.
[44] N.L. Okamoto, S. Fujimoto, Y. Kambara, M. Kawamura, Z.M.T. Chen, H. Matsunoshita, K. Tanaka, H. Inui, E.P. George, Size effect, critical resolved shear stress, stacking fault energy, and solid solution strengthening in the CrMnFeCoNi high-entropy alloy, Sci. Rep. 6 (2016) 35863.
[45] P.K.L.M. Komarasamy, N. Kumar, Z. Tang, R.S. Mishra, Effect of microstructure on the deformation mechanism of friction stir processed Al0.1CoCrFeNi high entropy alloy, Mater. Res. Lett. 3 (2015) 30–34.
[46] U.F. Kocks, H. Mecking, Physics and phenomenology of strain hardening: the FCC case, Prog. Mater. Sci. 48 (2003) 171–273.
[47] O. Bouaziz, N. Guelton, Modelling of TWIP effect on work-hardening, Mater. Sci. Eng. 319–321 (2001) 246–249.
[48] I. Gutierrez-Urrutia, D. Raabe, Dislocation and twin substructure evolution during strain hardening of an Fe-22 wt.% Mn-0.6 wt.% C TWIP steel observed by electron channeling contrast imaging, Acta Mater. 59 (2011) 6449–6462.
[49] O. Bouaziz, S. Allain, C.P. Scott, P. Cugy, D. Barbier, High manganese austenitic twinning induced plasticity steels: a review of the microstructure properties relationships, Curr. Opin. in Solid St. M. 15 (2011) 141–168.
[50] S.F. Liu, Y. Wu, H.T. Wang, W.T. Lin, Y.Y. Shang, J.B. Liu, K. An, X.J. Liu, H. Wang, Z.P. Lu, Transformation-reinforced high-entropy alloys with superior mechanical properties via tailoring stacking fault energy, J. Alloys Compd. 792 (2019) 444–455.
[51] A.K. De, J.G. Speer, D.K. Matlock, D.C. Murdock, M.C. Mataya, R.J. Comstock, Deformation-induced phase transformation and strain hardening in type 304 austenitic stainless steel, Metall. Mater. Trans. 37 (2006) 1875–1886.
[52] K.K. Spencer, M. Véron, Y. Zhang, J.D. Embury, The strain induced martensite transformation in austenitic stainless steels Part 1 - influence of temperature and strain history, Mater. Sci. Technol. 25 (2009) 7–17.